Identification of Coupled Landau and Anomalous Resonances in Space Plasmas

Jing-Huan Li,[1] Xu-Zhi Zhou,[1,*] Zhi-Yang Liu,[1,2] Shan Wang,[1] Anton V. Artemyev,[3] Yoshiharu Omura,[4] Xiao-Jia Zhang,[5] Li Li,[1] Chao Yue,[1] Qiu-Gang Zong,[1,6] Craig Pollock,[7] Guan Le,[8] and James L. Burch[9]

[1]*School of Earth and Space Sciences, Peking University, Beijing 100871, China*
[2]*Institut de Recherche en Astrophysique et Planétologie, CNES-CNRS, Universite Toulouse III, Paul Sabatier, Toulouse 31028, France*
[3]*Institute of Geophysics and Planetary Physics, University of California, Los Angeles, California 90095, USA*
[4]*Research Institute for Sustainable Humanosphere, Kyoto University, Kyoto 611-0011, Japan*
[5]*Department of Physics, University of Texas at Dallas, Richardson, Texas 75080, USA*
[6]*State Key Laboratory of Lunar and Planetary Sciences, Macau University of Science and Technology, Macau 999078, China*
[7]*Denali Scientific, Fairbanks, Alaska 99709, USA*
[8]*NASA Goddard Space Flight Center, Greenbelt, Maryland 20771, USA*
[9]*Southwest Research Institute, San Antonio, Texas 78238, USA*

(Received 27 October 2023; revised 5 May 2024; accepted 20 June 2024; published 16 July 2024)

Wave-particle resonance, a ubiquitous process in the plasma universe, occurs when resonant particles observe a constant wave phase to enable sustained energy transfer. Here, we present spacecraft observations of simultaneous Landau and anomalous resonances between oblique whistler waves and the same group of protons, which are evidenced, respectively, by phase-space rings in parallel-velocity spectra and phase-bunched distributions in gyrophase spectra. Our results indicate the coupling between Landau and anomalous resonances via the overlapping of the resonance islands.

DOI: 10.1103/PhysRevLett.133.035201

Introduction.—In collisionless space plasma environments, the dynamics of charged particles are largely governed by their interactions with plasma waves. The wave-particle energy transfer becomes especially efficient when they resonate, namely, the particle observes a constant wave phase. The resonance condition [1] in magnetized plasma is usually given by

$$\omega - k_{\parallel} v_{\parallel} = n\Omega, \tag{1}$$

where ω is the wave frequency, $k_{\parallel}$ is the parallel wave number, $v_{\parallel}$ is the particle's parallel velocity, Ω is the particle's gyrofrequency, and n is an integer. A fundamental resonant process, the Landau resonance, applies when $n = 0$ so that the particle moves at the same speed as the wave propagation along the background magnetic field to observe a constant phase $\phi_{E\parallel}$ of the wave parallel electric field $E_{\parallel}$. Another important resonance is the first-order cyclotron resonance, which occurs at $n = 1$ as the Doppler-shifted wave frequency matches the particle's gyrofrequency. Therefore, the phase difference ζ between the particle's perpendicular velocity and the wave magnetic field remains constant [2]. Accordingly, a resonant velocity [2] is defined as

$$V_r = (\omega - \Omega)/k_{\parallel} \tag{2}$$

to represent the parallel velocity of the particle in cyclotron resonance with the waves.

As a resonant particle gains or loses energy from the waves, its parallel velocity $v_{\parallel}$ also changes to deviate from the resonant velocity, which leads to the variation of wave-particle phase difference ($\phi_{E\parallel}$ for Landau resonance or ζ for cyclotron resonance). For some resonant particles, however, the $\phi_{E\parallel}$ or ζ variations are periodic to form closed particle trajectories in the $v_{\parallel} - \phi_{E\parallel}$ or $v_{\parallel} - \zeta$ phase space. This process is called nonlinear trapping, and the phase-space region occupied by the trapped particles is named resonance island [2–4]. These nonlinear wave-particle interactions play an important role in the dynamics of space environments. In the radiation belts, they are responsible for the frequency chirping of chorus waves [2,4] and the acceleration or precipitation of relativistic electrons [5,6]. In the foreshock solar wind, they produce gyrophase-bunched ions [7–9] and accelerate electron beams [10,11].

The cyclotron resonance can be further modified into anomalous resonance if the particle's gyromotion around the background magnetic field is significantly perturbed by the wave field, which changes the particle's angular velocity and thus revises the resonance condition (1) [12–16]. Moreover, the original resonance island can be dissociated into two separate islands when anomalous resonance occurs [16]. Interestingly, the Landau and anomalous [or cyclotron] resonances may occur simultaneously for oblique-propagating waves [17], although it remains unclear whether or how they are coupled.

Spacecraft identification of wave-particle resonance often relies on estimations of wave-particle energy transfer

[18–20] and/or averaged distributions of particles indicative of their diffusion processes [17,21–23]. Recently, the high-resolution particle observations from Magnetospheric Multiscale (MMS) spacecraft provide more detailed insights into particle dynamics within a single wave period. For instance, the observations of phase-bunched stripes in gyrophase spectra [24,25] and V-shaped structures in pitch-angle spectra [26] shed new light on nonlinear trapping of resonant particles in the wave field.

In this Letter, we use MMS observations to study the interactions between large-amplitude oblique whistler waves in the terrestrial foreshock and solar wind protons. In the parallel direction, a series of proton phase-space rings are observed with a one-to-one correspondence to $E_\parallel$ variations indicative of nonlinear Landau resonance. In the perpendicular plane, the periodic appearance of phase-bunched ion structures supports the occurrence of anomalous resonance. This is a direct observational identification of simultaneous Landau and anomalous resonances, and their coupling demonstrates the important roles of oblique waves in governing the complicated particle dynamics in space.

Observations.—Overview: At ~1630 UT on February 5, 2021, the four-spacecraft MMS constellation was located near the terrestrial bow shock at [13.7, 6.1, −6.1] R_E (Earth radius) in Geocentric Solar Eclipse (GSE) coordinates (with $\boldsymbol{x}$ axis toward the Sun and $\boldsymbol{z}$ axis perpendicular to the ecliptic plane). The onboard instruments offer high-resolution electromagnetic and particle measurements to analyze the wave-particle interactions [27–29]. In this event, the protons contribute over 99% to the plasma density, and we hereafter neglect the contribution of heavier ions.

Figure 1 provides a 1.5-hour overview of MMS3 observations. Similar features are also observed by other MMS satellites (not shown) due to their minor separations. The energy spectrum of ion energy fluxes in Fig. 1(a) indicates the back-and-forth crossings of the bow shock, characterized by the shifts between narrower and wider energy distributions that represent the foreshock solar wind and the thermalized magnetosheath ions, respectively. These features also agree with the higher and lower plasma bulk speeds in the foreshock and magnetosheath, respectively [see Fig. 1(b)]. The magnetic field B_y in Fig. 1(c) indicates the occurrence of ultralow-frequency waves at the period of 30–50s, which have been commonly reported in these regions [30–32].

Higher-frequency waves are also present in this event. Figure 1(d) shows the magnetic measurements from a 3-min segment, which exhibit oscillations with a decreasing wave period from 10 s to 4 s in the shadowed interval. The waves are also characterized by its large amplitude B_1, around 1.5 times the background field B_0. The shadowed interval is then chosen for in-depth analysis of wave properties and wave-ion interactions. Similar findings

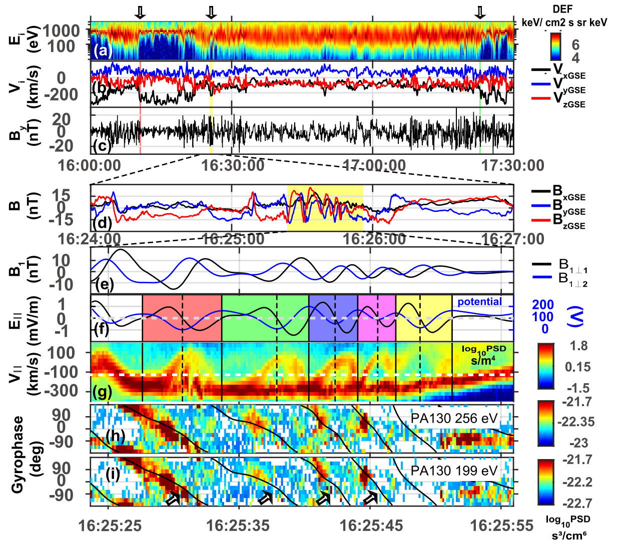

FIG. 1. MMS3 observations of oblique whistler waves. The top panels provide a 1.5-h overview, including (a) ion energy spectrum, (b) bulk velocity, and (c) magnetic field B_y. (d) A 3-min overview of magnetic field variations. The enlarged view of the shadowed interval is shown in the bottom panels, including (e) $\boldsymbol{B}_{1\perp}$, (f) $E_\parallel$, overplotted by the integrated potential. (g) $v_\parallel - t$ spectra. (h),(i) Gyrophase spectra. The black lines represent the gyrophase of $-\boldsymbol{B}_1$.

can also be drawn from observations near the red and green lines in Figs. 1(b) and 1(c), as detailed in the Supplemental Material [33].

Wave property: We first determine, based on the four-spacecraft measurements of the magnetic field, the wave vectors at each frequency [34]. The phase difference analysis [34], with details given in the Supplemental Material [33], provides the measured wave dispersion relation in the reference frame moving with the spacecraft, which can be further transformed into the plasma rest frame. This result reveals that the observed wave phase velocity $\boldsymbol{v}_w$ varies only slightly within the wave frequency range of interest, which is approximately $[-84.8 \pm 4.1, 32.0 \pm 5.0, 4.1 \pm 4.0]$ km/s. The estimated wave normal angle, approximately 150° between $\boldsymbol{v}_w$ and the background field $\boldsymbol{B}_0$, demonstrates an oblique wave propagation. The corresponding parallel wave numbers $k_\parallel$ range from $\sim -0.6/d_p$ to $\sim -1.5/d_p$, where $d_p \sim 100$ km is the proton inertial length. These estimations are further validated by the application of electromagnetic singular value decomposition analysis [35], which yields similar results (see the Supplemental Material [33] for details).

We further establish a field-aligned coordinate (FAC) with the parallel direction $\boldsymbol{e}_\parallel$ defined along $\boldsymbol{B}_0$, which is derived from a 15 s running average of the field measurements. In the perpendicular plane, the $\boldsymbol{e}_{\perp 1}$ direction is along the cross product of $\boldsymbol{B}_0$ and $\boldsymbol{v}_w$, and $\boldsymbol{e}_{\perp 2}$ completes the triad. Based on this coordinate, the particle gyrophase angle is defined by the angle between its perpendicular velocity $\boldsymbol{v}_\perp$

and the $e_{\perp 1}$ axis. The enlarged observations of the waves and the associated proton distributions, organized in the FAC coordinate, are shown in the bottom panels of Fig. 1. The perpendicular wave field $B_{1\perp}$, filtered from 0.1 to 0.3 Hz (close to proton gyrofrequency $f_{cp} \sim 0.3$ Hz), is displayed in Fig. 1(e). Obviously, its $\perp_2$ component leads its $\perp_1$ component in phase by $\pi/2$, which indicates a left-handed polarization. In the plasma rest frame, however, the waves propagate sunward at the speed of $[121.5 \pm 5.4, -45.9 \pm 6.9, -5.9 \pm 5.9]$ km/s, which indicates a polarization reversal into right-handed waves due to the Doppler effect (with a frequency around -1.4 rad/s) [26,32]. The waves are also associated with $E_\parallel$ oscillations [black line in Fig. 1(f)], and therefore, are identified as oblique whistler waves frequently reported in the foreshock [32,36].

Wave-proton interactions: To study the wave-proton interactions, we separate the time interval of interest into five wave periods [see the colored shadows in Fig. 1(f)] based on the electric-field phase angle $\phi_{E\parallel}$, which increases from 0° to 360° during each period. The dashed lines mark $\phi_{E\parallel} = 180°$, where the parallel electric potential [blue line in Fig. 1(f), integration of the observed $E_\parallel$] minimizes.

Figure 1(g) shows the ion phase-space density (PSD) distributions as functions of $v_\parallel$ and time, which display a series of rings with high PSDs surrounding their lower-PSD centers. All the ring centers are located near the potential minimum with $\phi_{E\parallel} \sim 180°$ (the dashed lines), and their parallel velocities ($v_\parallel \sim -100$ km/s) are close to the parallel wave speed $v_{w\parallel} = -105.0 \pm 4.3$ km/s. These five rings, as will be shown in the simulation section, represent the phase-space trajectories of the ions trapped within the wave-carried potential wells (the regions surrounding the potential minima), in which the ion parallel velocities vary between -300 and 100 km/s. The velocity variations, ± 200 km/s in the wave rest frame, are consistent with a 200-V potential well [shown in Fig. 1(f)] and the width of the Landau resonance island [1]. In other words, they are signatures of nonlinear Landau trapping for ions resonating with the whistler waves.

Interestingly, the same ion population is also modulated in the perpendicular plane. Figures 1(h)–1(i) show the gyrophase spectra of the 256- and 199-eV ions at the pitch-angle range of $130° \pm 20°$ (corresponding to a $v_\parallel$ range from -200 km/s to -100 km/s), which are characterized by periodic occurrences of inclined stripes with enhanced PSDs. Also shown in Figs. 1(h)–1(i) (as black lines) are the gyrophase of $-B_1$, which are mostly aligned with the inclined stripes to indicate the phase-bunched ion behavior at $\zeta \sim 180°$. These features are usually treated as diagnostic signatures of cyclotron resonance [24,25]. However, based on the wave properties given above, the cyclotron resonance velocity V_r is expected to be $\sim 108.7 \pm 58.8$ km/s, which differs dramatically from the parallel velocity of the phase-bunched ions.

The deviation from the classical cyclotron-resonance theory could be explained by the occurrence of anomalous resonance (also named anomalous trapping [15], distinctly different from anomalous cyclotron resonance [37]), which takes place when the wave-associated forces, including the $q\boldsymbol{v}_\parallel \times \boldsymbol{B}_1$ and $q\boldsymbol{E}_1$ forces in the perpendicular plane, are comparable to the background $q\boldsymbol{v}_\perp \times \boldsymbol{B}_0$ force. This is made possible by the comparable B_0 and B_1 magnitudes. The additional, wave-associated forces modify the conventional gyrofrequency Ω, and consequently, provide a new term in the classical condition (1) [15,16]. The resulting resonance speed (for ions at $\zeta = 180°$) [16] equals

$$V_r' = V_r - \frac{V_r - v_w}{k_\parallel v_\perp / \Omega_1 + 1}, \tag{3}$$

where V_r is obtained from Eq. (2), and $\Omega_1 = B_1 q/m$ is the nominal gyrofrequency associated with B_1. Based on Eq. (3), V_r' is estimated at approximately -200 km/s, corresponding to the pitch angle of $130° \pm 20°$ for 100–500 eV ions. Therefore, we speculate that the phase-bunched ion distributions in Figs. 1(h)–1(i) are caused by anomalous, rather than classical cyclotron, resonance. The observations suggest that oblique whistler waves could interact with the ions via Landau and anomalous resonances simultaneously, which will be examined through test-particle simulations.

Simulation.—We next follow the test-particle approach of Ref. [16] to study the interaction between oblique whistler waves and solar wind ions. In the simulation, the ion velocity distributions at any time and location are determined by tracing the ions backward in time, since Liouville's theorem requires PSD conservation along particle trajectories (see the Supplemental Material for detailed simulation setup [33]). The 3D distributions are integrated to obtain the $v_\parallel$-t and/or gyrophase spectrograms in the same format as observations in Figs. 1(g)–1(i).

Figure 2 shows virtual spacecraft observations of the simulated field and ion distributions since $t = t_0 + 45$ s. Figures 2(a) and 2(b) display the perpendicular wave magnetic field $B_{1\perp}$ and parallel electric field $E_\parallel$, respectively. Figure 2(c) shows the simulated $v_\parallel$-t spectrogram of

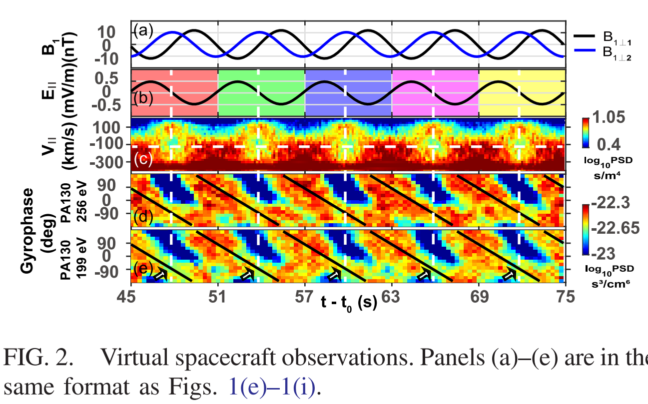

FIG. 2. Virtual spacecraft observations. Panels (a)–(e) are in the same format as Figs. 1(e)–1(i).

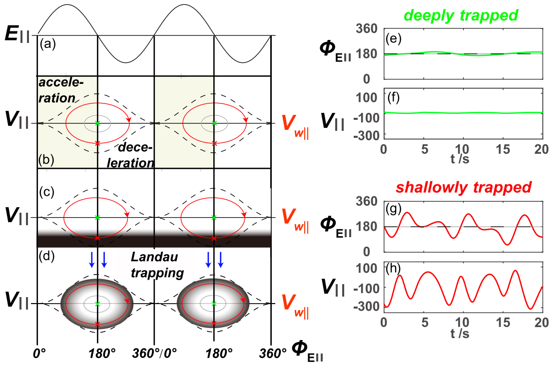

FIG. 3. Illustration of phase-space ring formation. (a) $E_{\parallel}$. (b) $v_{\parallel}$. (c) Initial $v_{\parallel}$ distribution, with black color denoting high PSDs. (d) Phase-mixing process. (e)–(h) $\phi_{E\parallel}$ and $v_{\parallel}$ variations for the green and red ions, respectively.

the ion PSDs, which resembles the periodic appearance of phase-space rings with a one-to-one correspondence to $E_{\parallel}$ variations in Fig. 2(b). The similarities between simulations and observations [compare Fig. 2(c) to Fig. 1(g)] enable us to understand the processes underlying the phase-space rings via analysis of the ion trajectories.

A schematic framework of our analysis is shown in Fig. 3. Here, the $E_{\parallel}$ profile is given in Fig. 3(a), with its phase angle $\phi_{E\parallel}$ increasing from 0° to 360° during each wave period. The corresponding electric potential minimizes at $\phi_{E\parallel} = 180°$, where the resonant ions are trapped nonlinearly [Landau trapping; see Fig. 3(b) for illustrations of closed trajectories in the $\phi_{E\parallel}$-$v_{\parallel}$ phase space]. The green ion in Fig. 3(b) is phase locked at the center of the potential well ($\phi_{E\parallel} = 180°$), which represents the deeply trapped ions with negligible $\phi_{E\parallel}$ and $v_{\parallel}$ variations. The wave-carried potential well can also trap the red ion in Fig. 3(b) despite larger variations in $\phi_{E\parallel}$ and $v_{\parallel}$. Since its trajectory is close to the separatrix of the resonance island, the ion belongs to the shallowly trapped population.

The initial PSDs for deeply and shallowly trapped ions are distinctly different, however. The initial ion distributions in [33] indicate PSD peaks at $v_{\parallel} \sim -370$ km/s (the background solar wind), which is much lower than $v_{w\parallel}$ and thus is located near the bottom of the $\phi_{E\parallel}$-$v_{\parallel}$ diagram in Fig. 3(c) (the black region, which represents the background ion concentration). Since the trajectories of the deeply trapped ions (including the green ion) cannot intersect the high-PSD region, the phase space occupied by these ions (the resonance island center) can only have lower densities due to the PSD conservation. The shallowly trapped ions, however, have trajectories intersecting the black region (the red trajectories) so that the high-PSD solar wind ions can easily access the outer edge of the resonance islands. Note that there are also regions with low initial PSDs along the red trajectories, and therefore, it would take longer than a Landau trapping period for the ions with higher and lower PSDs to mix in phase space and produce rings with intermediately high PSDs [Fig. 3(d)]. Here, the Landau-trapping period of ~6 s is indeed shorter than the formation time (~30 s) of phase-space rings in the simulations.

To examine the scenario of phase-space ring formation via Landau trapping, we launch two typical ions for their trajectories in the modeled field. The green ion trajectory in Figs. 3(e) and 3(f) shows minor oscillations of $\phi_{E\parallel}$ and $v_{\parallel}$ around 180° and −100 km/s (approximately the parallel wave velocity $v_{w\parallel}$), respectively. Their minor variations indicate that the ion belongs to the deeply trapped population. On the other hand, the red ion experiences a larger variation of $\phi_{E\parallel}$ from ~90° to ~270° [Fig. 3(g)], which indicates that it is trapped, albeit more shallowly, within the potential well (otherwise, $\phi_{E\parallel}$ should cover the full range from 0° to 360°). Moreover, its $v_{\parallel}$ changes significantly from ~ -300 km/s to ~100 km/s [Fig. 3(h)], which indicates that solar-wind ions with higher PSDs can indeed be transported in phase space along closed trajectories around the resonance island. Therefore, we conclude that the formation of phase-space ion rings is associated with particle trapping, serving as the observational identification of nonlinear Landau resonance.

We next return to the simulated ion gyrophase spectra [Figs. 2(d) and 2(e)], which reproduce the phase-bunched features in observations [Figs. 1(h)–1(i)]. To confirm that the phase-bunched features are caused by anomalous resonance, we show in Fig. 4(a) the $v_{\parallel} - \zeta$ portrait of the ion phase-space trajectories. Here, for simplicity, we assume field-aligned wave propagation, with the effect of oblique propagation to be discussed later on. There are two resonance islands occupying different $v_{\parallel}$ ranges, centered at $\zeta = 0°$ (purple lines) and $\zeta = 180°$ (blue lines), respectively [16]. The blue island centered at $\zeta = 180°$ corresponds to lower $v_{\parallel}$ values. Therefore, the nearby ion trajectories, including the closed (blue) and the traversing trajectories (yellow), can access the background solar-wind ions ($v_{\parallel} \sim -370$ km/s), which leads to the concentration of high-PSD ions around the $\zeta = 180°$ island. Figure 4(a) also displays the observed $v_{\parallel} - \zeta$ spectrum (averaged from 1625:33.7 to 1625:35.7), in which the high-PSD ions are indeed concentrated around $\zeta = 180°$. This scenario is consistent with the superimposed trajectories, contributing to the inclined stripes in observations [Figs. 1(h)–1(i)] and simulations [Figs. 2(d) and 2(e)].

Discussion and summary.—The simulated ion trajectories in oblique waves could be more complicated than expected from the $v_{\parallel} - \zeta$ diagram. Figure 4(b) shows the ζ variations of a sample ion, which switches back and forth between traversing (when ζ varies monotonically from 360° to 0°) and trapped trajectories (when ζ oscillates around $\zeta = 0°$ or 180°) within either island. The switch between

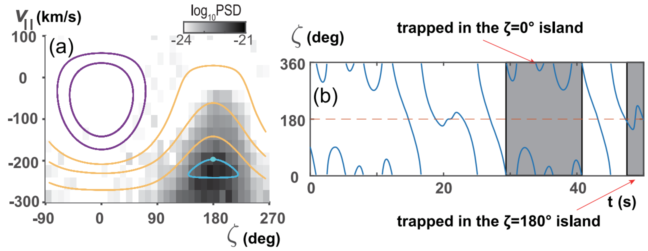

FIG. 4. Typical particle trajectories in the simulation. (a) The $v_{\parallel} - \zeta$ spectrum, overplotted by ion trajectories. (b) ζ variation.

different types of trajectories is usually attributed to field variations [2,16], but this is not the case here. Instead, the reason lies in the existence of $E_{\parallel}$ (a property of oblique whistler waves), which perturbs the parallel ion motion in the $v_{\parallel} - \zeta$ diagram and consequently destabilizes the ion trajectories. As a result, the phase-bunched stripes in Figs. 1(i) and 2(e) are not homogeneous, with minimum PSDs near $\phi_{E\parallel} \sim 180°$ [see arrows in Figs. 1(i) and 2(e)] where the ions are Landau trapped by $E_{\parallel}$ [see the white dashed lines in Fig. 2(c), corresponding to the low-PSD centers].

In other words, the Landau and anomalous resonances are largely coupled. This coupling process, in analogy to the coupling between Landau and cyclotron resonances [38,39], is caused by the coexistence of the $q\boldsymbol{E}_{\parallel}$ and $q\boldsymbol{V}_{\perp} \times \boldsymbol{B}_{\perp}$ forces in the parallel direction, and more importantly, the overlapped resonance islands in the $v_{\parallel}$ range between -300 km/s and 100 km/s. The coupling does not only affect the anomalous resonance; the Landau resonance can also be perturbed by the $q\boldsymbol{v}_{\perp} \times \boldsymbol{B}_{\perp}$ force, although in our case, the $q\boldsymbol{v}_{\perp} \times \boldsymbol{B}_{\perp}$ force is much smaller than $q\boldsymbol{E}_{\parallel}$ due to the ion concentration at $\zeta = 180°$. Consequently, the disturbances in Figs. 1(g) and 2(c) are much weaker. This additional force, however, could still revise the particle trapping period to expedite the phase-mixing process in the ring formation [1].

In summary, we demonstrate the simultaneous occurrence of Landau and anomalous resonances between oblique whistler waves and solar wind ions. The two resonant processes are strongly coupled through the overlapped resonance islands, which is made possible by the coexistence of wave-associated electric and Lorentz forces in the parallel direction. For anomalous resonance, the ion trapping and traversing behavior are perturbed by the additional electric force, which obscures the characteristic, phase-bunched features. The diagnostic signatures for Landau resonance [phase-space rings in Figs. 1(g) and 2(c)], however, are perturbed only slightly by the wave-associated Lorentz force due to the ion concentration near $\zeta = 180°$. As the coupling strengthens, more chaotic ion motion and more complicated features could be expected, which may further revise the picture of foreshock wave-particle energy transfer. This is beyond the scope of this paper, and we will carry out a more systematic study to better understand the coupling process.

This work was supported by the National Natural Science Foundation of China, Grant No. 42174184. We are grateful to the MMS mission for the high-resolution measurements. The MMS data were processed and analyzed using the IRFU-Matlab package.

*Contact author: xzzhou@pku.edu.cn

[1] D. Nunn and Y. Omura, A computational and theoretical investigation of nonlinear wave-particle interactions in oblique whistlers, J. Geophys. Res. **120**, 2890 (2015).
[2] Y. Omura, Nonlinear wave growth theory of whistler-mode chorus and hiss emissions in the magnetosphere, Earth, Planets Space **73**, 95 (2021).
[3] A. V. Artemyev, A. A. Vasiliev, D. Mourenas, O. V. Agapitov, and V. V. Krasnoselskikh, Electron scattering and nonlinear trapping by oblique whistler waves: The critical wave intensity for nonlinear effects, Phys. Plasmas **21**, 102903 (2014).
[4] X. Tao, F. Zonca, L. Chen, and Y. Wu, Theoretical and numerical studies of chorus waves: A review, Sci. China Earth Sci. **63**, 78 (2020).
[5] J. C. Foster, P. J. Erickson, Y. Omura, D. N. Baker, C. A. Kletzing, and S. G. Claudepierre, Van Allen probes observations of prompt MeV radiation belt electron acceleration in nonlinear interactions with VLF chorus, J. Geophys. Res. **122**, 324 (2017).
[6] X.-J. Zhang, A. Artemyev, V. Angelopoulos, E. Tsai, C. Wilkins, S. Kasahara, D. Mourenas, S. Yokota, K. Keika, T. Hori, Y. Miyoshi, I. Shinohara, and A. Matsuoka, Superfast precipitation of energetic electrons in the radiation belts of the earth, Nat. Commun. **13**, 1611 (2022).
[7] M. Hoshino and T. Terasawa, Numerical study of the upstream wave excitation mechanism: 1. Nonlinear phase bunching of beam ions, J. Geophys. Res. **90**, 57 (1985).
[8] C. Mazelle, K. Meziane, D. LeQuèau, M. Wilber, J. Eastwood, H. Rème, J. Sauvaud, J. Bosqued, I. Dandouras, and M. McCarthy, Production of gyrating ions from nonlinear wave-particle interaction upstream from the Earth's bow shock: A case study from cluster-CIS, Planet. Space Sci. **51**, 785 (2003).
[9] N. Romanelli, C. Mazelle, and K. Meziane, Nonlinear wave-particle interaction: Implications for newborn planetary and backstreaming proton velocity distribution functions, J. Geophys. Res. **123**, 1100 (2018).
[10] A. V. Artemyev, X. Shi, T. Z. Liu, X. J. Zhang, I. Vasko, and V. Angelopoulos, Electron resonant interaction with whistler waves around foreshock transients and the bow shock behind the terminator, J. Geophys. Res. **127**, e2021JA029820 (2022).
[11] X. Shi, A. Artemyev, V. Angelopoulos, T. Liu, and X.-J. Zhang, Evidence of electron acceleration via nonlinear resonant interactions with whistler-mode waves at foreshock transients, Astrophys. J. **952**, 38 (2023).

[12] J. M. Albert, A. V. Artemyev, W. Li, L. Gan, and Q. Ma, Models of resonant wave-particle interactions, J. Geophys. Res. **126**, e2021JA029216 (2021).

[13] A. Artemyev, A. Neishtadt, J. Albert, L. Gan, W. Li, and Q. Ma, Theoretical model of the nonlinear resonant interaction of whistler-mode waves and field-aligned electrons, Phys. Plasmas **28**, 052902 (2021).

[14] J. Bortnik, J. M. Albert, A. Artemyev, W. Li, C. Jun, V. S. Grach, and A. G. Demekhov, Amplitude dependence of nonlinear precipitation blocking of relativistic electrons by large amplitude EMIC waves, Geophys. Res. Lett. **49**, e2022GL098365 (2022).

[15] M. Kitahara and Y. Katoh, Anomalous trapping of low pitch angle electrons by coherent whistler mode waves, J. Geophys. Res. **124**, 5568 (2019).

[16] J.-H. Li, Z.-Y. Liu, X.-Z. Zhou, L. Li, Y. Omura, C. Yue, Q.-G. Zong, Z.-Y. Pu, S.-Y. Fu, L. Xie, C. T. Russell, C. J. Pollock, G. Le, and J. L. Burch, Anomalous resonance between low-energy particles and electromagnetic plasma waves, Commun. Phys. **5**, 300 (2022).

[17] E. Behar, F. Sahraoui, and L. Berčič, Resonant whistler-electron interactions: MMS observations versus test-particle simulation, J. Geophys. Res. **125**, e2020JA028040 (2020).

[18] C. Chen, K. Klein, and G. G. Howes, Evidence for electron Landau damping in space plasma turbulence, Nat. Commun. **10**, 740 (2019).

[19] A. Afshari, G. Howes, C. Kletzing, D. Hartley, and S. Boardsen, The importance of electron Landau damping for the dissipation of turbulent energy in terrestrial magnetosheath plasma, J. Geophys. Res. **126**, e2021JA029578 (2021).

[20] K. G. Klein, G. G. Howes, J. M. TenBarge, and F. Valentini, Diagnosing collisionless energy transfer using field–particle correlations: Alfvén-ion cyclotron turbulence, J. Plasma Phys. **86**, 905860402 (2020).

[21] J. He, L. Wang, C. Tu, E. Marsch, and Q. Zong, Evidence of Landau and cyclotron resonance between protons and kinetic waves in solar wind turbulence, Astrophys. J. Lett. **800**, L31 (2015).

[22] T. A. Bowen, B. D. G. Chandran, J. Squire, S. D. Bale, D. Duan, K. G. Klein, D. Larson, A. Mallet, M. D. McManus, R. Meyrand *et al.*, In situ signature of cyclotron resonant heating in the solar wind, Phys. Rev. Lett. **129**, 165101 (2022).

[23] M. D. McManus, K. G. Klein, S. D. Bale, T. A. Bowen, J. Huang, D. Larson, R. Livi, A. Rahmati, O. Romeo, J. Verniero *et al.*, Proton-and alpha-driven instabilities in an ion cyclotron wave event, Astrophys. J. **961**, 142 (2024).

[24] N. Kitamura, M. Kitahara, M. Shoji, Y. Miyoshi, H. Hasegawa, S. Nakamura, Y. Katoh, Y. Saito, S. Yokota, D. J. Gershman, A. F. Vinas, B. L. Giles, T. E. Moore, W. R. Paterson, C. J. Pollock, C. T. Russell, R. J. Strangeway, S. A. Fuselier, and J. L. Burch, Direct measurements of two-way wave-particle energy transfer in a collisionless space plasma, Science **361**, 1000 (2018).

[25] Z. Y. Liu, Q. G. Zong, R. Rankin, H. Zhang, Y. F. Wang, X. Z. Zhou, S. Y. Fu, C. Yue, X. Y. Zhu, C. J. Pollock, S. A. Fuselier, and G. Le, Simultaneous macroscale and microscale wave-ion interaction in near-Earth space plasmas, Nat. Commun. **13**, 5593 (2022).

[26] Z. Y. Liu, B. Wang, Q. G. Zong, S. T. Yao, C. J. Pollock, and G. Le, Thermal electron behavior in obliquely propagating whistler waves: MMS observations in the solar wind, Geophys. Res. Lett. **48**, e2021GL094099 (2021).

[27] C. Pollock *et al.*, Fast plasma investigation for magnetospheric multiscale, Space Sci. Rev. **199**, 331 (2016).

[28] R. B. Torbert *et al.*, The fields instrument suite on MMS: Scientific objectives, measurements, and data products, Space Sci. Rev. **199**, 105 (2016).

[29] D. T. Young *et al.*, Hot plasma composition analyzer for the magnetospheric multiscale mission, Space Sci. Rev. **199**, 407 (2014).

[30] M. Hoppe, C. Russell, L. Frank, T. Eastman, and E. Greenstadt, Upstream hydromagnetic waves and their association with backstreaming ion populations: ISEE 1 and 2 observations, J. Geophys. Res. **86**, 4471 (1981).

[31] M. M. Hoppe and C. T. Russell, Plasma rest frame frequencies and polarizations of the low-frequency upstream waves: ISEE 1 and 2 observations, J. Geophys. Res. **88**, 2021 (1983).

[32] L. B. Wilson III, Low frequency waves at and upstream of collisionless shocks, in *Low-Frequency Waves in Space Plasmas*, edited by A. Keiling, D.-H. Lee, and V. Nakariakov (American Geophysical Union, 2016), 10.1002/9781119055006.ch16.

[33] See Supplemental Material at http://link.aps.org/supplemental/10.1103/PhysRevLett.133.035201 for the parameters, setting the electromagnetic fields and particle distributions in the simulation.

[34] T. Dudok de Wit, V. Krasnosel'skikh, S. Bale, M. Dunlop, H. Lühr, S. Schwartz, and L. Woolliscroft, Determination of dispersion relations in quasi-stationary plasma turbulence using dual satellite data, Geophys. Res. Lett. **22**, 2653 (1995).

[35] O. Santolík, M. Parrot, and F. Lefeuvre, Singular value decomposition methods for wave propagation analysis, Radio Sci. **38**, 1010 (2003).

[36] M. Hoppe and C. Russell, Whistler mode wave packets in the Earth's foreshock region, Nature (London) **287**, 417 (1980).

[37] Y. Omura and Q. Zhao, Nonlinear pitch angle scattering of relativistic electrons by EMIC waves in the inner magnetosphere, J. Geophys. Res. **117**, A08227 (2012).

[38] G. R. Smith and A. N. Kaufman, Stochastic acceleration by a single wave in a magnetic field, Phys. Rev. Lett. **34**, 1613 (1975).

[39] G. R. Smith and A. N. Kaufman, Stochastic acceleration by an obliquely propagating wave—an example of overlapping resonances, Phys. Fluids **21**, 2230 (1978).